

Case History

Polynomial-based density inversion of gravity anomalies for concealed iron-deposit exploration in North China

Jie Liu¹, Jianzhong Zhang², Li Jiang¹, Qi Lin³, and Li Wan¹

ABSTRACT

Inversion of residual gravity anomalies is an important geophysical technique for depicting subsurface density contrasts, for example, for mineral deposits. We have expressed subsurface density variations using depth-variable polynomial functions and developed the polynomial coefficient inversion (PCI) method, which is an alternative method for mapping subsurface density distributions by inverting the coefficients of density-contrast functions. PCI enables the linear inversion of density variations without vertically subdividing the subsurface. Synthetic tests indicate

that PCI combines polynomial functions and multiple constraints to highlight the anomalous masses through an iterative process with appropriate weighting parameters. We apply our method to a local investigation of banded iron formation (BIF) deposits in the Hebei Province, North China. The inversion results depict the approximate distribution of the subsurface density contrasts to identify the stratigraphic boundaries of different lithologies and BIF-favorable zones, thus implying that local iron-rich ore bodies may be located at the syncline axis or dip along the faults. The successful application of PCI for the BIF deposits indicates that this method is a promising strategy for density mapping.

INTRODUCTION

A gravity anomaly is a type of geophysical response caused by the distribution of density contrasts in the subsurface, and gravity inversion plays a role in detecting subsurface geologic structures and concealed targets in mineral exploration (Carlos et al., 2014; Xiao and Wang, 2017). In general, gravity inversion techniques can be divided into two categories: geometric inversions (e.g., Silva et al., 2006; Døssing et al., 2014) and density-contrast inversions (e.g., Bertete-Aguirre et al., 2002). Assuming that the subsurface density distribution is known, geometric inversions are used to determine the boundaries of subsurface bodies or the depths of interfaces, such as the basement of a basin (Guan et al., 2016) or a deep discontinuity (Shin et al., 2009). Density-contrast inver-

sions are used to determine the subsurface density-contrast distributions to identify fault zones and deep magmatic intrusions or to delineate shallow dike complexes and ore bodies (Fournier et al., 2004; Flinders et al., 2013).

Density-contrast inversion techniques usually divide the subsurface into cells with horizontal and vertical grids, and the density contrast in each cell is assumed to be constant. Gravity anomalies are inverted for the density contrasts among all cells by minimizing an objective function of the measured and predicted data (this approach is generally known as direct inversion). The objective function is often composed of the data misfit defined by the L₂-norm, prior information, and smoothness constraint functions (Li and Oldenburg, 1998). Additional constraints, such as the L₁-norm and minimum-support constraint, are also introduced into the inversion

Manuscript received by the Editor 26 October 2018; revised manuscript received 15 March 2019; published ahead of production 14 May 2019; published online 12 August 2019.

¹Ocean University of China, Key Lab of Submarine Geosciences and Prospecting Techniques, MOE, College of Marine Geosciences, Qingdao 266100, China. E-mail: liujieouc@126.com; jianglifzb@163.com; wanli.mail@foxmail.com.

²Ocean University of China, Key Lab of Submarine Geosciences and Prospecting Techniques, MOE, College of Marine Geosciences, Qingdao 266100, China and Qingdao National Laboratory for Marine Science and Technology, Evaluation and Detection Technology Laboratory of Marine Mineral Resources, Qingdao 266061, China. E-mail: zhangjz@ouc.edu.cn.

³Qingdao National Laboratory for Marine Science and Technology, Evaluation and Detection Technology Laboratory of Marine Mineral Resources, Qingdao 266061, China. E-mail: linqiqd@163.com.

© 2019 Society of Exploration Geophysicists. All rights reserved.

to better reflect the boundaries of mass bodies (Last and Kubik, 1983; Portniaguine and Zhdanov, 1999; Zhdanov et al., 2004; Commer, 2011). Based on spatially gridded cells, the inversion kernel is related to the gravity response calculated by summing the effects of all constant-density cells, which is often a time-consuming process (Jiang et al., 2017).

Considering the variable densities of most real geologic bodies, several researchers have deduced analytical expressions of gravity anomalies of masses in which the density varies with depth or/and lateral positions (Guspi, 1990; Zhang et al., 2001; Zhou, 2010; D'Urso, 2015; Wu and Chen, 2016; Jiang et al., 2017, 2018; Zhang and Jiang, 2017; Chen et al., 2018; Wu, 2018a, 2018b), which have enabled the development of gravity forward calculations of variable density without meshing. Special tests were performed by Jiang et al. (2017) to quantitatively analyze the computation resources required by two forward strategies (polynomial-based analytic expression and summing the effects of uniform subprisms), and the results indicated that the analytical solution based on polynomials can improve the efficiency and accuracy of the forward calculations of gravity anomalies of variable density-contrast bodies compared with summation of the effects of a collection of uniform prisms, especially when the number of prisms is large.

Guspi (1990) inverts for the basement depth of a basin under the assumption that the density varies with depth as a fifth-order polynomial function. Subsequently, variable density has been widely used in geometric inversions, i.e., the first category of gravity inversion (Barbosa et al., 1999; Chakravarthi and Sundararajan, 2004, 2007; Silva et al., 2006; Martins et al., 2010). To the best of our knowledge, however, previous studies have not reported density-contrast inversions using an arbitrary-order polynomial function, which belongs to the second category of gravity inversion.

Based on the analytic expressions of gravity anomalies caused by a collection of horizontal rectangular prisms with the arbitrary-order polynomial density, we propose a density-contrast inversion method by determining the polynomial coefficients from residual gravity anomalies, which is referred to as the polynomial coefficient inversion (PCI) method. In the following sections, the PCI method is first described and tested by a synthetic case. Then, the method is applied to the gravity anomaly data for a banded iron formation (BIF) exploration in the Hebei Province, China.

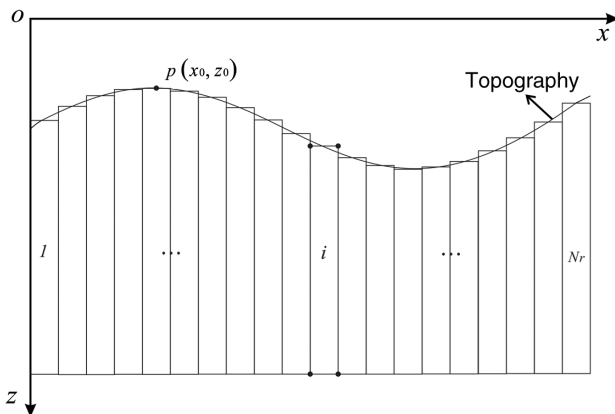


Figure 1. The subdivision of the subsurface into N_r rectangular elements without vertical meshes. All elements have the same depth. Point p represents an observation position on the surface.

METHODOLOGY

Gravity solution

The subsurface is divided into a set of 2D vertically juxtaposed rectangular elements (Figure 1). The density-contrast variation of each element is expressed as a polynomial function of depth, and the density contrast of the i th element at depth z can be expressed as follows:

$$\rho(i, z) = \sum_{j=0}^{N_z} a_{i,j} z^j, \quad i = 1, 2, \dots, N_r, \quad (1)$$

where N_z is the maximum order of z , $a_{i,j}$ is the coefficient of term z^j of the density-contrast function in the i th element, and N_r is the number of rectangular elements.

The gravity anomaly at any point $p(x_0, z_0)$ on a surface along the x -axis caused by the i th vertical rectangular element can be expressed as (Zhang et al., 2001)

$$\Delta g_i(x_0, z_0) = 2G \sum_{j=0}^{N_z} a_{i,j} \iint_{S_i} \frac{z^j (z - z_0)}{(x - x_0)^2 + (z - z_0)^2} dx dz, \quad (2)$$

where G is the gravitational constant. The gravity anomaly at point p caused by all single vertical rectangular elements is

$$\Delta g(x_0, z_0) = \sum_{i=1}^{N_r} \sum_{j=0}^{N_z} f(x_0, z_0, i, j) a_{i,j}, \quad (3)$$

where

$$f(x_0, z_0, i, j) = 2G \iint_{S_i} \frac{z^j (z - z_0)}{(x - x_0)^2 + (z - z_0)^2} dx dz. \quad (4)$$

Efforts have been made to convert the 2D areal integral in equation 4 to a 1D line integral (Zhang et al., 2001; Zhou, 2008, 2009). The analytic expression of equation 4 is given in Appendix A. If N_m gravity-observation points exist, then we obtain the following from equation 3:

$$\Delta \mathbf{g}_{N_m \times 1} = \mathbf{F}_{N_m \times (N_z+1)N_r} \mathbf{a}_{(N_z+1)N_r \times 1}, \quad (5)$$

where $\mathbf{a}_{(N_z+1)N_r \times 1}$ is the polynomial coefficient matrix, $\Delta \mathbf{g}_{N_m \times 1}$ represents the gravity anomalies observed at N_m points, and $\mathbf{F}_{N_m \times (N_z+1)N_r}$ is the gravity kernel matrix, whose elements are derived in equation 4 (see Appendix A). For the inversion problem discussed below, \mathbf{F} and $\Delta \mathbf{g}$ denote the known quantities, whereas \mathbf{a} should be solved to map the density contrasts.

Polynomial coefficient inversion

Objective function

Unconstrained gravity inversions inherently yield nonunique solutions. An effective method of reducing this nonuniqueness is to impose various constraints (e.g., Li and Oldenburg, 1998; Silva

et al., 2001; Ghalehnoee et al., 2017). For PCI, we combine bound constraints, regularization, and depth and focusing weightings to establish an objective function to produce a stable optimal solution by an iterative process. The objective function is given by

$$\varphi(\mathbf{a}) = \|\mathbf{W}_d(\mathbf{F}\mathbf{a} - \Delta\mathbf{g})\|_2^2 + \lambda_1 \|\mathbf{C}_m \mathbf{C}_d \mathbf{P}\mathbf{a}\|_2^2 + \lambda_2 \|\mathbf{R}\mathbf{a}\|_2^2, \quad (6)$$

where the first term denotes the data misfit, the second term is the a priori term (here, a zero model is used without external a priori density), the third term represents the spatial regularization term, λ_1 and λ_2 are the weighting coefficients of the corresponding terms, $\mathbf{W}_d = \text{diag}\{1/\sigma_1, 1/\sigma_2, \dots, 1/\sigma_{N_m}\}$ is the data-weighting matrix, and σ_i is the standard deviation of the noise in the i th datum. The other parameters in the constraint terms are described below.

Bound and regularization

The density contrast of the i th rectangular element at depth z_k can be denoted by the product of $[1 \ z_k \ \dots \ z_k^{N_z}]$ and $[a_{i,0} \ a_{i,1} \ \dots \ a_{i,N_z}]^T$. To express the density contrasts among all elements at different depths z_k ($k = 1, 2, \dots, K$, where K denotes the number of depth constraint points for each element), we construct a diagonal block matrix $\mathbf{P} = \text{diag}\{\mathbf{P}_1, \mathbf{P}_2, \dots, \mathbf{P}_{N_r}\}$, and $\mathbf{P}_1, \mathbf{P}_2, \dots, \mathbf{P}_{N_r}$ can be unified as follows:

$$\mathbf{P}_1 = \mathbf{P}_2 = \dots = \mathbf{P}_{N_r} = \begin{bmatrix} 1 & z_1 & \dots & z_1^{N_z} \\ 1 & z_2 & \dots & z_2^{N_z} \\ \vdots & \vdots & \ddots & \vdots \\ 1 & z_K & \dots & z_K^{N_z} \end{bmatrix}. \quad (7)$$

Therefore, $\mathbf{P}\mathbf{a}$ can represent the density contrasts among different horizontal positions and depths. The term $\rho_{\min} \leq \mathbf{P}\mathbf{a} \leq \rho_{\max}$ is imposed on the inversion process, where ρ_{\min} and ρ_{\max} are the lower and upper bounds of the density contrasts, respectively. The choice of depth range is determined by the depth of interest. The interval for the depth constraint ranges from 0.01 to 1 km according to the depth range. Similarly, spatial regularization is imposed on the density contrasts between adjacent positions to constrain the relative amplitude by second-order differential operators \mathbf{R} . For example, the horizontal differential matrix of the density contrast can be expressed as

$$\begin{bmatrix} -\mathbf{P}_1 & 2\mathbf{P}_2 & -\mathbf{P}_3 & & & \\ & -\mathbf{P}_2 & 2\mathbf{P}_3 & -\mathbf{P}_4 & & \\ & & \ddots & \ddots & \ddots & \\ & & & -\mathbf{P}_{N_r-2} & 2\mathbf{P}_{N_r-1} & -\mathbf{P}_{N_r} \end{bmatrix}. \quad (8)$$

Depth weighting

Various depth weightings have been proposed to counteract the influence of attenuation on the gravity kernel function with depth (Li and Oldenburg, 1998; Commer, 2011). The term $\mathbf{C}_d = \text{diag}\{c_{d(i,k)}\}$ ($i = 1, 2, \dots, N_r; k = 1, 2, \dots, K$) in equation 6 is a diagonal matrix of depth weightings, and its elements are related to depth and expressed as follows:

$$c_{d(i,k)} = \frac{1}{(z_k + z_0)^{\beta/2}}, \quad (9)$$

where β is usually equal to two and z_0 is determined to allow the best match between the decay of the sensitivity and the square of the weighting function (Li and Oldenburg, 1996). In general, incorporation of factual information about the sources, such as the approximate location of the true source top, is required for desired source enhancement (Barbosa et al., 2002).

Focusing weighting

Tikhonov regularization usually produces a diffuse image, and compact or focusing constraints help to generate clearer images for geologic structures with sharper borders (Last and Kubik, 1983; Portniaguine and Zhdanov, 1999; Zhdanov et al., 2004; Commer, 2011). We referred to Portniaguine and Zhdanov (2002) to construct an iterative inversion process by changing the weights of the model space in each step. The term $\mathbf{C}_m = \text{diag}\{c_{m(i,k)}\}$ ($i = 1, 2, \dots, N_r; k = 1, 2, \dots, K$) in equation 6 is a diagonal matrix of focusing weightings whose elements are expressed as follows:

$$c_{m(i,k)} = \frac{1}{(\rho_{ik}^2 + \gamma^2)^{1/2}}, \quad (10)$$

where ρ_{ik} represents the density of the i th rectangular element at depth z_k in the preceding iteration and γ is a small value that prevents meaningless denominators.

Parameter selection and procedure

The maximum order N_z of polynomials determines the density complexity of the inversion. A trade-off is observed between the number of inversion unknowns and the resolution; that is, a smaller polynomial degree and smaller number of rectangular elements correspond to greater efficiency but poorer density-contrast estimate resolution. According to the different resolution requirements, the lateral width of the rectangles is generally set to 0.5–2 times the observation spacing. Higher order polynomials can simulate greater density variations. To select the maximum order, Jiang et al. (2017) demonstrate that eighth-order polynomials can effectively model abrupt density variations. Therefore, while considering the calculation efficiency, we take N_z in the range of 8–11.

Selecting weighting factors is also an important step. For the first inversion because no inversion result is available as a reference, \mathbf{C}_m in equation 6 is initialized to an identity matrix. At this point, the last two terms of equation 6 can be combined into one and $\lambda_1 = \lambda_2$. Thus, the first inversion can be viewed as a conventional L_2 -norm inversion with only one weighting. This weighting parameter is used to balance the data misfit and model roughness. We use the classic L-curve method (Hansen, 1992) to determine an appropriate value.

After the first inversion, we obtain a smooth density model. In the subsequent iteration, \mathbf{C}_m is calculated in equation 10 using the density model obtained in the last iteration, and the previous inversion is used as a constraint to compress the model size and increase the model focus. At this time, the second term with focusing information in equation 6 should be considered separately from the regularization term. To obtain the appropriate value of λ_1 , we fix the

regularization weighting λ_2 determined in the first inversion; thus, the L-curve method is similarly executed to obtain an optimal compromise between the model structure and data misfit.

After determining the weightings, the optimization problem with linear inequality constraints at each iteration is solved by an active-set method (Gill et al., 1984).

SYNTHETIC DATA TESTS

To illustrate the general flow and validate the PCI method, a synthetic model is designed. The model is composed of two positive (0.3 g/cm^3) and two negative (-0.3 g/cm^3) density masses with different sizes and depths (Figure 2b). The anomalies of the vertical component of gravity, consisting of 120 measurement points distributed at a distance of 0–8 km along the horizontal line with equal

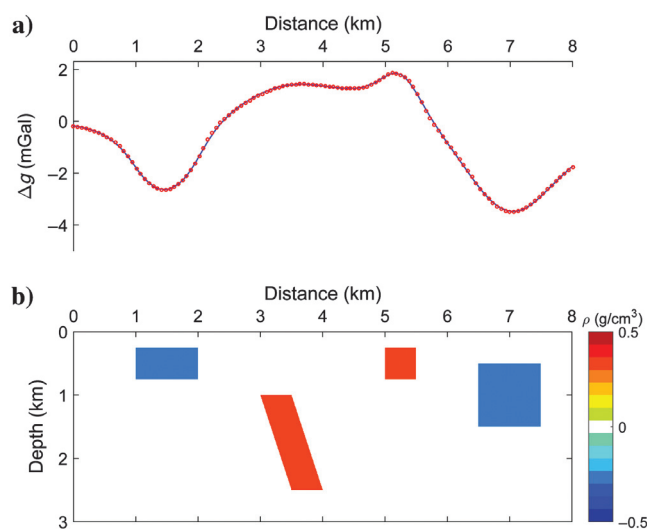


Figure 2. Theoretical gravity anomalies with noise (a, the solid line) caused by the synthetic model (b) and calculated gravity anomalies (a, the red circles) from the final inversion model (Figure 6d).

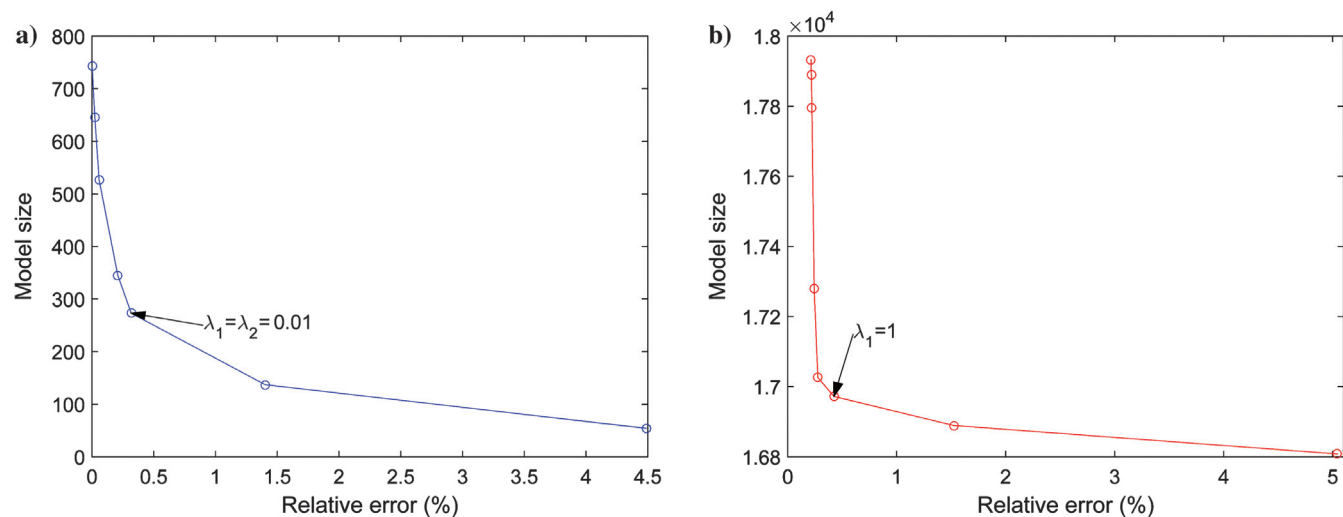


Figure 3. (a) The L-curve of the first inversion with $\lambda_1 = \lambda_2 = 0.0001, 0.0005, 0.001, 0.005, 0.01, 0.05, \text{ and } 0.1$. (b) L-curve of the first iteration with $\lambda_2 = 0.01$ and $\lambda_1 = 0.001, 0.01, 0.1, 0.3, 0.5, 1, 3, \text{ and } 7$.

spacing, are calculated using analytical formulas, and Gaussian random noise with a zero mean and a standard deviation of 0.01 mGal is added (Figure 2a, the solid line).

To implement the PCI method, the subsurface is equidistantly divided into 60 vertical rectangles with the same depth range of 0–3 km, and the depth-variable density contrast is expressed using a ninth-order polynomial function (i.e., $N_z = 9$). The upper and lower bounds of the density contrast are set to 0.5 and -0.5 g/cm^3 , respectively. For each vertical rectangle element, 300 points evenly spaced in depth are used as constraint points. Depth-weighting factor β is set to two by trial. Before solving this linearized objective function, suitable weighting parameters λ_1 and λ_2 must be determined.

Weighting selection by L-curves

For the first inversion, the two weighting parameters are combined into one. We try seven weighting values of 0.0001, 0.0005, 0.001, 0.005, 0.01, 0.05, and 0.1 and calculate the data misfits and relevant model sizes via inversion. The model size is obtained by counting the number of density points whose absolute value is greater than a threshold ρ_t among the 60×300 constraint positions (for the first inversion, $\rho_t = 0.1 \text{ g/cm}^3$, and for the subsequent iterations, ρ_t is a smaller value of 0.0001 g/cm^3).

Figure 3a shows the relationship between the relative errors of the data fit and model sizes for the first inversion using different weightings. Figure 4 shows the models inverted for the first time and the corresponding data residuals when the weighting equals 0.001, 0.01, and 0.1. When the weighting is small, the data fit better with large model roughness (Figure 4a and 4b), whereas a high weighting factor leads to a smoother model but with overt deviations in the data fit (Figure 4e and 4f). According to the L-curve shown in Figure 3a, we determine that $\lambda_1 = \lambda_2 = 0.01$ for the first inversion. As a result, the absolute error level of the data fit is equivalent to the added Gaussian white noise (Figure 4d), and the relative error is below 0.5% (Figure 3a). The initial inverted model is relatively diffuse, and the magnitude of the density contrast is lower than that of the real model (Figure 4c). Furthermore, due to the presence of

positive and negative anomalies, the inversion results show a smooth lateral transition between positive and negative density contrasts, which are more pronounced in the shallow layers.

For the second inversion (i.e., the first iteration), we fix $\lambda_2 = 0.01$ and set the weighting λ_1 equal to 0.001, 0.01, 0.1, 0.3, 0.5, 1, 3, and 7. Figure 3b shows the L-curve, and Figure 5 shows the density models and data residuals for the first iteration when λ_1 equals 0.01, 1, and 7. The model differences generated by weightings at different scales are similar to those of the first inversion. According to the “L” plot, we assign the focusing weighting factor $\lambda_1 = 1$ in subsequent iterations. This weighting can effectively minimize the size of the model structure while ensuring that the data-fit error is within 0.5%.

Results analysis versus iteration results

After the weighting factors are determined, we perform 20 iterations. Before each iteration, the focusing constraint matrix C_m is updated using the last inverted model. Figure 6 shows the model inverted after 2, 4, 10, and 20 iterations. To evaluate the inversion results, we calculate the mean absolute error (MAE) of the model and the average density update (ADU) at each iteration. The MAE is defined as the total absolute value of the errors between the inverted model at the current iteration and the real model divided by the number of total points. The ADU is defined as the total absolute deviation of the inverted model at the current iteration from the last iteration divided by the number of total points.

Figure 7 shows the MAE and ADU values of the inversion models, which vary based on the number of iterations. As the number of iterations increases, the ADU gradually decreases along with the MAE. In practice, the iteration can be stopped by judging whether the ADU is less than a certain threshold or if the maximum number of iterations has been reached. After 10 iterations, the results tend to converge. The final model is consistent with the real model with regard to position and volume, and the boundaries of the mass bodies are clearer. The gravity anomalies (Figure 2a, the red circle) calculated using the final inversion model (Figure 6d) sufficiently match the theoretical anomalies. These tests indicate the feasibility of the PCI method.

APPLICATION TO A LOCAL BIF

Geologic setting

A BIF is a type of sedimentary metamorphic iron ore formed during the Precambrian (mainly from the Archean to the Paleoproterozoic) and represents one of the most important types of iron ore deposits, which are widely distributed throughout North China (Han et al., 2014). Our study area is a local BIF zone belonging to the

eastern block of the North China Craton (NCC) in the Hebei Province. It is mostly covered by Quaternary pluvial-alluvial sediments, and it has a flat terrain. Below the Quaternary overburden is the Proterozoic Changcheng System and the Archean Qianxi Group metamorphic rock series. The Archean strata outcrops in the northern study area and the Changcheng System strata outcrops in the south with the Quaternary strata at different scales (Figure 8a). A combination of field investigations and sample mineral analyses revealed the compositions of the rocks and their densities (see Table 1).

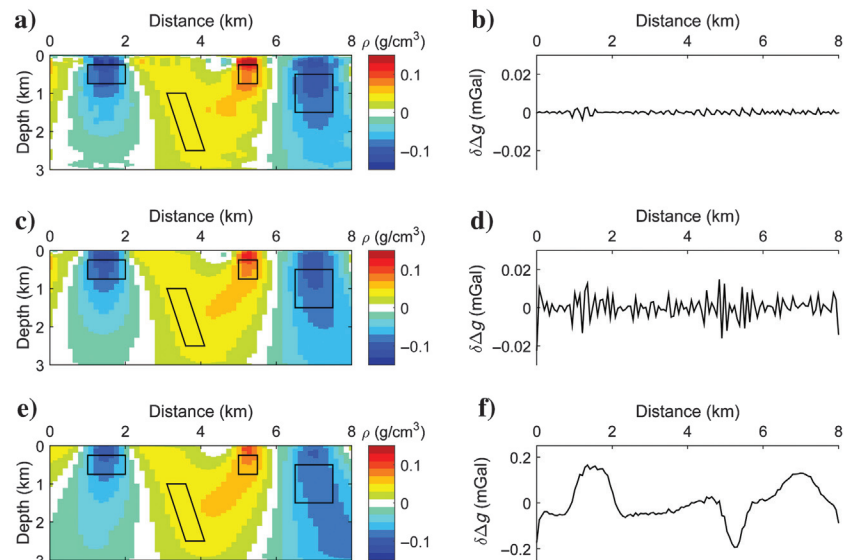


Figure 4. Density models of the first inversion (a, c, and e) and the corresponding data fit errors (b, d, and f), with $\lambda_1 = \lambda_2 = 0.001, 0.01$, and 0.1 , respectively. The black lines on the density models show the real positions of the mass bodies. The first inversion indicates the result using a conventional L_2 -norm method without focusing constraints.

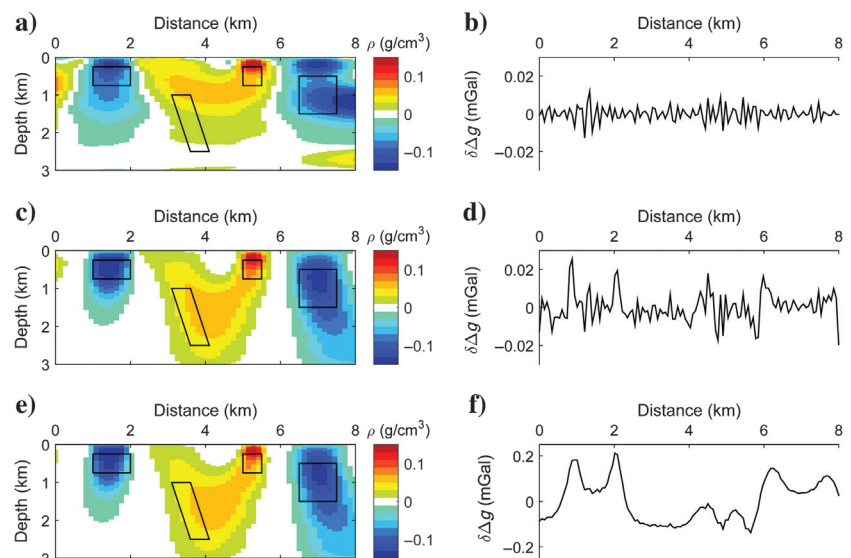


Figure 5. Density models of the first iteration (a, c, and e) and the corresponding data fit errors (b, d, and f), with fixed values of $\lambda_2 = 0.01$ and $\lambda_1 = 0.01, 1$, and 7 , respectively. The black lines on the density models show the real positions of the mass bodies.

As shown in Table 1, the Quaternary sediments are composed of loose materials with the lowest densities. The density of dolomite in the Gaoyuzhuang Formation is relatively high, whereas the

densities of the other formations in the Changcheng System, which mainly consist of quartzite and quartz sandstone, are relatively low. The Archean Qianxi Group can be divided into the Malanyu Formation and the Santunying Formation. The main lithologies of the Qianxi Group are described as follows:

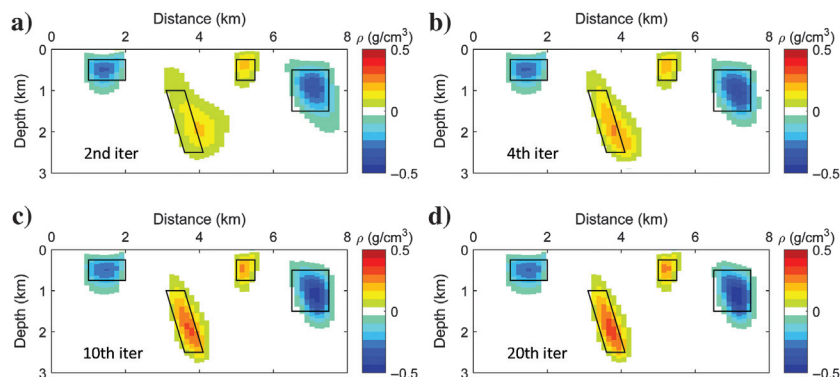


Figure 6. Density models inverted at the (a) 2nd, (b) 4th, (c) 10th, and (d) 20th iterations. The black lines on the density models show the real positions of the mass bodies. The final inversion with iterative focusing displays better results than only the L_2 -norm constraint shown in Figure 4c.

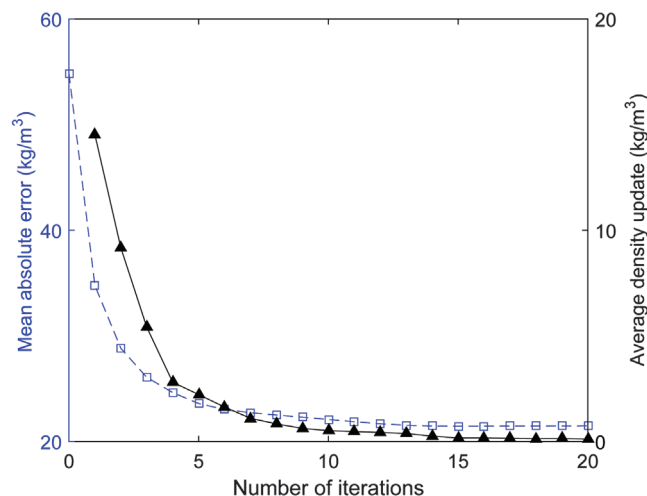


Figure 7. The MAE and ADU values of the inversion models versus the number of iterations.

1) Biotite-amphibole-plagiogneiss: This lithology is the Archean main host rock in our study area, and it has an ash black heteromorphic crystalloblastic texture and gneiss structure. The main mineral composition consists of plagioclase, pyroxene (hypersthene) quartz, amphibolite, and biotite. These rocks generally present various degrees of migmatization, which manifests in felsic veins that penetrate along the schistosity and form strips of migmatization.

2) Granulite: This lithology is not widely distributed, usually at the top and bottom of iron ores or near them and sometimes in a transitional relationship with iron ores. The main minerals are pyroxene, plagioclase, and garnet.

3) BIF: Ore minerals of the BIFs are dominated by magnetite. The BIFs mainly appear stratiform or stratoid in the biotite-amphibole-plagiogneiss, and a local branching phenomenon can be observed.

Above all, the densities of the Archean Qianxi Group rocks are the highest compared with those of the formations of the Changcheng System, and the average density contrast exceeds 0.3 g/cm^3 (Table 1).

Ore-body characteristics of proven iron deposits

A proven BIF deposit is located near the village of XSC, which is shown as the XSC BIF zone in Figure 8a, and a partial enlarged plane view is shown in Figure 8b.

According to the distribution of iron ore, the XSC BIF zone is roughly divided into four groups (M1–M4), with M4 having the greatest length. The drilling results revealed that M2, which is located in the eastern part of the XSC BIF zone, is the ore body with the largest thickness and greatest quantity of ore beds. M2 extends

Table 1. Composition and density characteristics of the lithologic series within the study area from different eras.

Era	Period/Group/Formation		Symbol	Lithology	Density range (g/cm^3)	Density mean (g/cm^3)
Cenozoic	Quaternary		Q	Loose materials	1.70–2.13	2.05
Proterozoic	Changcheng System	Gaoyuzhuang	Chg	Dolomite	2.15–3.03	2.75
		Dahongyu	Chd	Quartzite	2.62–2.71	2.67
		Tuanshanzi	Cht			
		Chuanlinggou	Chch	Quartz sandstone	2.54–2.62	
Archean	Qianxi Group	Changzhougou	Chc			
		Malanyu	Arm	Biotite-amphibole-plagiogneiss	2.62–2.82	2.98
		Santunying	Ars	Granulite	2.52–2.80	
				BIF	2.52–3.44	

570 m in length, strikes northeast at 20° , dips northwest with an angle of 30° – 40° , and has a total thickness of 100 m and a maximum depth greater than 450 m. Except for the XSC BIF zone, most of the study area remains relatively unexplored. The discovery of more concealed iron ore bodies by geophysical investigation and geologic interpretation is strongly anticipated.

Gravity anomalies

High-precision gravity measurements covering the whole study area (approximately 100 km^2) were performed to further prospect for concealed ore bodies. The gravity measurement network was designed as regular rectangles with an interval of 0.25 km. The total root-mean-square error for the gravity measurements was estimated at $\pm 0.15 \text{ mGal}$. To study the distribution of shallow orebodies, the residual gravity anomaly (Figure 9) was separated from the regional background field using a wavelet transform and multi-scale analysis method (Hou and Yang, 2011).

As shown in Figure 9, in the central study area, the residual gravity anomaly shows an obvious strip-shaped high-gravity anomaly in the east–west direction with three local peak areas. The area of high-gravity anomalies corresponds to the Quaternary cover in Figure 8a. The position distribution of a potential BIF cannot be determined from geologic investigation alone. In reality, the high-gravity anomalies in the Quaternary cover indicate a high probability of concealed BIF deposits in the Qianxi Group beneath the Quaternary strata. Because of the flat terrain and relatively simple shallow structure of the study area, the measurement points are almost on a horizontal plane and we implement a convenient 2D inversion to detect the distribution of potential BIF deposits by the PCI method.

Inversion and interpretation

Six lines with typical gravity anomalies are selected at a certain distance (Figure 9). Using the PCI method, the left and right edges of the inversion region along each profile are expanded outward by 2 km to avoid potential edge effects. The width of the rectangles is taken as 0.7 times the observation spacing (i.e., a total of 80 upright rectangles equidistantly with a maximum depth of 1.2 km). The density-contrast variations with depth are expressed using 10th-order polynomial functions.

Figure 10 shows the inversion results for each profile (the part of the edge expansion is not displayed). Obvious positive density anomalies are observed within the Archean Qianxi Group compared with the density background of the Proterozoic Changcheng System. The Quaternary cover is composed of loose materials and exhibits a negative density anomaly. According to these characteristics and the plane geologic map, the boundary between these different eras is drawn by the dotted lines (Figure 10b, 10c, 10e, and 10f). Line B–B' passes through the XSC iron ore. The inversion of line B–B' shows that the density contrasts greater than 0.25 g/cm^3 beneath XSC exhibit a narrow striped distribution (Figure 10b) with an average thickness of 100 m, a horizontal extent of 1 km, and a

maximum depth of 500 m, which is consistent with the drilling results.

In addition, large positive density-contrast anomalies are detected along profiles A–A', C–C', E–E', and F–F' (Figure 10a, 10c, 10e, and 10f) corresponding to three high-magnitude gravity anomaly zones in the middle of the study area (Figure 9). These anomalies are mainly caused by density contrasts between the Proterozoic Changcheng System strata and the Archean Qianxi Group BIF deposits. The negative densities at the right edge correspond to the observed negative gravity anomalies, which may indicate a thickening of the Quaternary sediment or be related to incomplete separation of

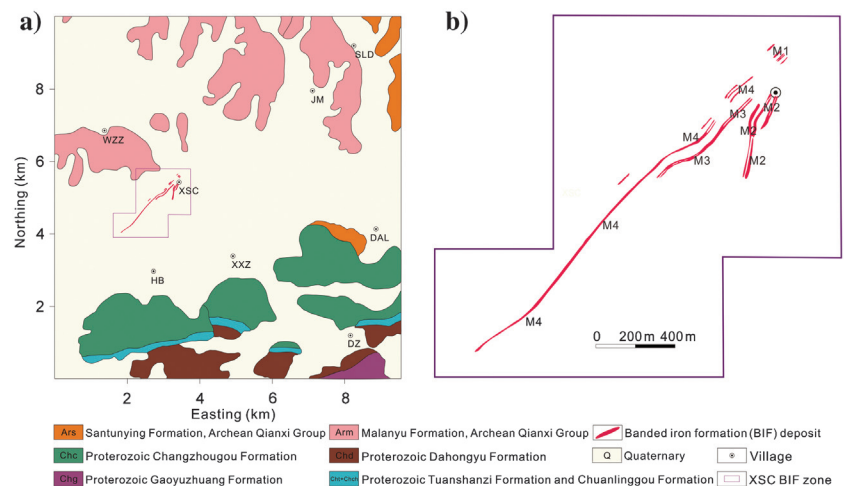


Figure 8. (a) Geologic map of the study area. Villages are represented by acronyms for simplification. (b) Partially enlarged plane view of the proven XSC BIF zone.

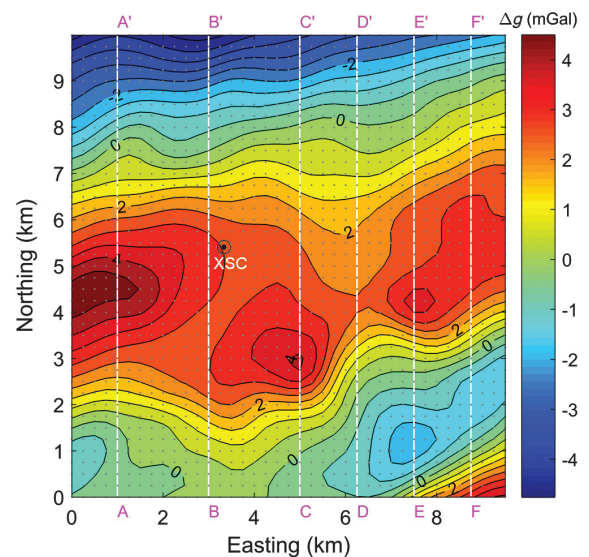


Figure 9. Residual gravity anomalies of the study area (after subtracting the regional field). The gray points show station locations. The positive gravity anomaly indicates the presence of a high-density body extending east–west that is concentrated over a north–south distance of 2–7 km. The white lines labeled as A–A' ($X = 1 \text{ km}$), B–B' ($X = 3 \text{ km}$), C–C' ($X = 5 \text{ km}$), D–D' ($X = 6.25 \text{ km}$), E–E' ($X = 7.5 \text{ km}$), and F–F' ($X = 8.75 \text{ km}$) pass through the positive anomaly with typical gravity anomaly characteristics.

residual anomalies. Furthermore, the zones that are favorable for the formation of BIFs are delineated, indicating substantial prospecting potential in the study area (Figure 10a, 10c, 10e, and 10f).

Implications related to BIFs

Archean metamorphic strata are widely developed in the study area. The original BIFs formed in the Precambrian marine volcanic sedimentary formation and iron minerals were dominated by magnetite (Zhang et al., 2012). The iron-ore mineralization in this area is directly related to the Archean-Paleoproterozoic volcanic eruption-sedimentation event. Due to the strong tectonic and magmatic activity at approximately 2.5 Ga in the NCC (Zhang et al., 2011; Han et al., 2014), the iron ore was generally subjected to intense transformation and deformation. Uplift and erosion increase the difficulty of retaining BIFs. In the deformation process of the fold structure, the syncline is advantageous for preserving the ore body, possibly causing partial thickening of the ore body.

Figure 10 shows that the local positive density contrast can reach more than 0.4 g/cm^3 , indicating the probable existence of local deep iron-rich deposits. The iron-rich deposits are subdivided by genesis into the original deposit type and later-stage tectonic-hydrothermal transformation type. The latter type suffers from the effects of tectonism, metamorphism, and migmatization (Zhang et al., 2012). Our results indicate that the local iron-rich ores may be influenced by the geologic structure located in the fold axis (Figure 10a) or extended along the dip controlled by faults (Figure 10e and 10f).

Anatexis and local migmatization lead to a relationship of gradual change and transition between the iron ores and host rocks (Zhang et al., 2012; Li et al., 2015). In this case, the observed geophysical anomalies also include the contribution of the surrounding host rocks. The gravity inversion method can facilitate the identification of the lithologic boundaries of different periods with a certain density contrast (Figure 10b, 10c, 10e, and 10f) and generally delineate potential deposits. Although other geophysical data are limited, our results reveal a key indicator of concealed BIFs. For further comprehensive interpretation of deep ore-controlling structures, a combination of geologic analysis with multiple geophysical data and drilling is needed.

CONCLUSION

We have proposed a new density-contrast inversion method based on arbitrary-order polynomial density functions. Multiple mathematical constraints introduced into the inversion process coinciding with geologic information reduce nonuniqueness and improve the reliability of the inversion. Synthetic tests show the validity of the method for local body detection.

We successfully applied the method to the exploration of BIFs in North China. The BIF detected within the study area belongs to a typical sedimentary metamorphic iron-ore deposit, and it is hosted within the biotite-amphibole-plagiogneiss of the Qianxi Group. According to the density contrasts among the Quaternary, the Proterozoic Changcheng System, and the Archean, the lithologic boundaries between the different eras were delineated.

In addition, the BIF-favorable zones were distinguished. Our results indicate that iron-rich deposits are potentially localized in the fold axis and dip along the fault due to tectonism, metamorphism, or migmatization.

Although the description of the spatial distribution of density contrasts by a polynomial limits the solution to a class of smooth functions, by implementing a focusing constraint, local density variations can also be inverted. Under conditions in which density gradually changes with compaction, such as sediments filling basins, the polynomial density approximation is expected to work better. This work focuses on gravity inversion with no prior knowledge in the early stage of exploration. In this case, gravity inversion tends to recover a minimum structure model. For more complex density modeling (such as the vertical superposition of positive and negative density bodies), a combination of a priori models or multiple data is needed. The error of our results may be derived from the 2D assumptions or incomplete anomaly separation. However, based on the gravity forward solution of density-variable prisms, future 3D extensions of the proposed approach should be straightforward.

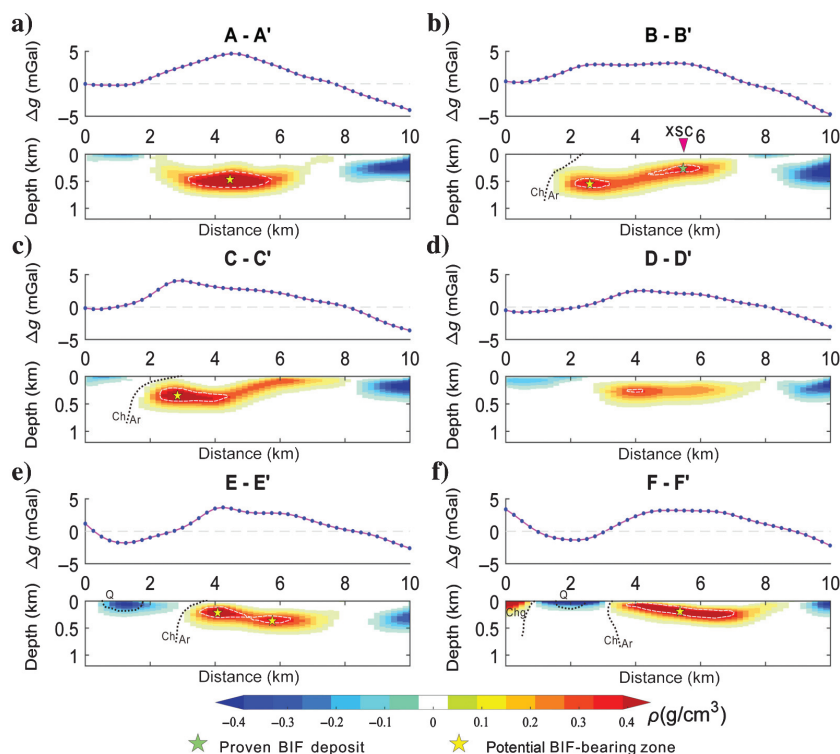


Figure 10. Gravity inversion results for the six lines. The distributions of ore bodies under profiles B-B', E-E', and F-F' have distinguishing dipping features. The density contrasts delineate the boundaries among the Archean, Proterozoic, and Quaternary strata (shown as the black dotted lines). The density-contrast contours greater than 0.25 g/cm^3 are encircled by the dashed white lines. Potential BIF-bearing zones are accordingly depicted along the profiles by the yellow stars.

ACKNOWLEDGMENTS

We sincerely thank the associate editor, assistant editor D. Draganov, reviewers M. Burianyk, ed. K. Biegert, and two anonymous reviewers for

their thoughtful comments that helped us improve this paper. This work was supported by the National Key Research and Development Program of China (grant no. 2018YFC0603600) and the Key R&D Program of Shandong Province, China (grant no. 2017GSF16103).

DATA AND MATERIALS AVAILABILITY

Data associated with this research are confidential and cannot be released.

APPENDIX A

FORMULATION OF THE GRAVITY KERNEL MATRIX

Using the Stokes' theorem and the right-hand rule, a complete set of closed-form expressions was obtained for computing gravity anomalies when the density contrast varies as a polynomial function. Based on the solution transformation method described by Zhou (2010), a simplified form of equation 4 can be rewritten as

$$f(x_0, z_0, i, j) = -2G \sum_{m=0}^j \frac{1}{j-m+1} C_j^m(z_0)^m \sum_{k=1}^4 E_i(j, m, k), \quad (\text{A-1})$$

where C_j^m is the binomial expansion coefficients and $E_i(j, m, k)$ is the integral along the k th segment counterclockwise from vertex (x_k, z_k) to vertex (x_{k+1}, z_{k+1}) of the i th element. The term $E_i(j, m, k)$ is given by

$$E_i(j, m, k) = \begin{cases} (x_k - x_0) K_{j-m+1}, & \text{if } x_k = x_{k+1} \\ -(z_k - z_0)^{j-m+2} I_0, & \text{if } x_k \neq x_{k+1}, \text{ and } z_k \neq z_0 \\ 0, & \text{if } x_k \neq x_{k+1}, \text{ and } z_k = z_0 \end{cases}, \quad (\text{A-2})$$

where

$$K_\ell = \begin{cases} \frac{1}{2} \ln \left[\frac{(x_{k+1} - x_0)^2 + (z_{k+1} - z_0)^2}{(x_k - x_0)^2 + (z_k - z_0)^2} \right], & \ell = 1 \\ (z_{k+1} - z_k) - |x_k - x_0| \left(\arctan \frac{z_{k+1} - z_0}{|x_k - x_0|} - \arctan \frac{z_k - z_0}{|x_k - x_0|} \right), & \ell = 2 \\ \frac{1}{\ell-1} [(z_{k+1} - z_0)^{\ell-1} - (z_k - z_0)^{\ell-1}] - (x_k - x_0)^2 K_{\ell-2}, & \ell > 2 \end{cases}, \quad (\text{A-3})$$

and

$$I_0 = \frac{1}{|z_k - z_0|} \left(\arctan \frac{x_{k+1} - x_0}{|z_{k+1} - z_0|} - \arctan \frac{x_k - x_0}{|z_k - z_0|} \right). \quad (\text{A-4})$$

Thus, the elements in $\mathbf{F}_{N_m \times (N_z+1)N_r}$ are given as

$$\mathbf{F}_{N_m \times (N_z+1)N_r} = \begin{bmatrix} f(x_1, z_1, 1, 0) & \cdots & f(x_1, z_1, 1, N_z) & \cdots & f(x_1, z_1, N_r, 0) & \cdots & f(x_1, z_1, N_r, N_z) \\ f(x_2, z_2, 1, 0) & \cdots & f(x_2, z_2, 1, N_z) & \cdots & f(x_2, z_2, N_r, 0) & \cdots & f(x_2, z_2, N_r, N_z) \\ \vdots & \vdots & \vdots & \vdots & \vdots & \ddots & \vdots \\ f(x_{N_m}, z_{N_m}, 1, 0) & \cdots & f(x_{N_m}, z_{N_m}, 1, N_z) & \cdots & f(x_{N_m}, z_{N_m}, N_r, 0) & \cdots & f(x_{N_m}, z_{N_m}, N_r, N_z) \end{bmatrix}. \quad (\text{A-5})$$

REFERENCES

- Barbosa, V. C., J. B. Silva, and W. E. Medeiros, 1999, Stable inversion of gravity anomalies of sedimentary basins with nonsmooth basement reliefs and arbitrary density contrast variations: *Geophysics*, **64**, 754–764, doi: [10.1190/1.1444585](https://doi.org/10.1190/1.1444585).
- Barbosa, V. C., J. B. Silva, and W. E. Medeiros, 2002, Practical applications of uniqueness theorems in gravimetry — Part 2: Pragmatic incorporation of concrete geologic information: *Geophysics*, **67**, 795–800, doi: [10.1190/1.1484523](https://doi.org/10.1190/1.1484523).
- Bertete-Aguirre, H., E. Cherkaev, and M. Oristaglio, 2002, Non-smooth gravity problem with total variation penalization functional: *Geophysical Journal International*, **149**, 499–507, doi: [10.1046/j.1365-246X.2002.01664.x](https://doi.org/10.1046/j.1365-246X.2002.01664.x).
- Carlos, D. U., L. Uieda, and V. C. Barbosa, 2014, Imaging iron ore from the Quadrilátero Ferrífero (Brazil) using geophysical inversion and drill hole data: *Ore Geology Reviews*, **61**, 268–285, doi: [10.1016/j.oregeorev.2014.02.011](https://doi.org/10.1016/j.oregeorev.2014.02.011).
- Chakravarthi, V., and N. Sundararajan, 2004, Ridge-regression algorithm for gravity inversion of fault structures with variable density: *Geophysics*, **69**, 1394–1404, doi: [10.1190/1.1836814](https://doi.org/10.1190/1.1836814).
- Chakravarthi, V., and N. Sundararajan, 2007, 3D gravity inversion of basement relief — A depth-dependent density approach: *Geophysics*, **72**, no. 2, I23–I32, doi: [10.1190/1.2431634](https://doi.org/10.1190/1.2431634).
- Chen, C., Z. Ren, K. Pan, J. Tang, T. Kalscheuer, H. Maurer, Y. Sun, and Y. Li, 2018, Exact solutions of the vertical gravitational anomaly for a polyhedral prism with vertical polynomial density contrast of arbitrary orders: *Geophysical Journal International*, **214**, 2115–2132, doi: [10.1093/gji/ggy250](https://doi.org/10.1093/gji/ggy250).
- Commer, M., 2011, Three-dimensional gravity modelling and focusing inversion using rectangular meshes: *Geophysical Prospecting*, **59**, 966–979.
- Døssing, A., T. M. Hansen, A. V. Olesen, J. R. Hopper, and T. Funck, 2014, Gravity inversion predicts the nature of the Amundsen Basin and its continental borderlands near Greenland: *Earth and Planetary Science Letters*, **408**, 132–145, doi: [10.1016/j.epsl.2014.10.011](https://doi.org/10.1016/j.epsl.2014.10.011).
- D'Urso, M. G., 2015, The gravity anomaly of a 2D polygonal body having density contrast given by polynomial functions: *Surveys in Geophysics*, **36**, 391–425, doi: [10.1007/s10712-015-9317-3](https://doi.org/10.1007/s10712-015-9317-3).
- Flinders, A. F., G. Ito, M. O. Garcia, J. M. Sinton, J. Kauahikaua, and B. Taylor, 2013, Intrusive dike complexes, cumulate cores, and the extrusive growth of Hawaiian volcanoes: *Geophysical Research Letters*, **40**, 3367–3373, doi: [10.1002/grl.50633](https://doi.org/10.1002/grl.50633).
- Fournier, N., H. Rymer, G. Williams-Jones, and J. Brenes, 2004, High-resolution gravity survey: Investigation of subsurface structures at Poás volcano, Costa Rica: *Geophysical Research Letters*, **31**, L15602.
- Ghalehnoee, M. H., A. Ansari, and A. Ghorbani, 2017, Improving compact gravity inversion using new weighting functions: *Geophysical Journal International*, **208**, 546–560, doi: [10.1093/gji/ggw413](https://doi.org/10.1093/gji/ggw413).
- Gill, P. E., W. Murray, M. A. Saunders, and M. H. Wright, 1984, Procedures for optimization problems with a mixture of bounds and general linear constraints: *ACM Transactions on Mathematical Software (TOMS)*, **10**, 282–298, doi: [10.1145/1271.1276](https://doi.org/10.1145/1271.1276).
- Guan, D., X. Ke, and Y. Wang, 2016, Basement structures of East and South China Seas and adjacent regions from gravity inversion: *Journal of Asian Earth Sciences*, **117**, 242–255, doi: [10.1016/j.jseae.2015.12.017](https://doi.org/10.1016/j.jseae.2015.12.017).
- Guspi, F., 1990, General 2D gravity inversion with density contrast varying with depth: *Geoprospection*, **26**, 253–265, doi: [10.1016/0016-7142\(90\)90007-F](https://doi.org/10.1016/0016-7142(90)90007-F).
- Han, C., W. Xiao, B. Su, Z. Chen, X. Zhang, S. Ao, J. Zhang, Z. Zhang, B. Wan, D. Song, and Z. Wang, 2014, Neoproterozoic Algoma-type banded iron formations from Eastern Hebei, North China Craton: SHRIMP U-Pb age, origin and tectonic setting: *Precambrian Research*, **251**, 212–231, doi: [10.1016/j.precamres.2014.06.019](https://doi.org/10.1016/j.precamres.2014.06.019).
- Hansen, P. C., 1992, Analysis of discrete ill-posed problems by means of the L-curve: *SIAM Review*, **34**, 561–580, doi: [10.1137/1034115](https://doi.org/10.1137/1034115).
- Hou, Z., and W. Yang, 2011, Multi-scale inversion of density structure from gravity anomalies in Tarim Basin (in Chinese with English abstract): *Science China Earth Sciences*, **54**, 399–409.
- Jiang, L., J. Liu, J. Zhang, and Z. Feng, 2018, Analytic expressions for the gravity gradient tensor of 3D prisms with depth-dependent density: *Surveys in Geophysics*, **39**, 337–363, doi: [10.1007/s10712-017-9455-x](https://doi.org/10.1007/s10712-017-9455-x).
- Jiang, L., J. Zhang, and Z. Feng, 2017, A versatile solution for the gravity anomaly of 3D prism-meshed bodies with depth-dependent density contrast: *Geophysics*, **82**, no. 4, G77–G86, doi: [10.1190/geo2016-0394.1](https://doi.org/10.1190/geo2016-0394.1).
- Last, B. J., and K. Kubik, 1983, Compact gravity inversion: *Geophysics*, **48**, 713–721, doi: [10.1190/1.1441501](https://doi.org/10.1190/1.1441501).
- Li, L. X., H. M. Li, Y. X. Xu, J. Chen, T. Yao, L. F. Zhang, X. Q. Yang, and M. J. Liu, 2015, Zircon growth and ages of migmatites in the Algoma-type BIF-hosted iron deposits in Qianxi Group from Eastern Hebei Province, China: Timing of BIF deposition and anatexis: *Journal of Asian Earth Sciences*, **113**, 1017–1034, doi: [10.1016/j.jseae.2015.02.007](https://doi.org/10.1016/j.jseae.2015.02.007).

- Li, Y., and D. W. Oldenburg, 1996, 3-D inversion of magnetic data: *Geophysics*, **61**, 394–408, doi: [10.1190/1.1443968](https://doi.org/10.1190/1.1443968).
- Li, Y., and D. W. Oldenburg, 1998, 3-D inversion of gravity data: *Geophysics*, **63**, 109–119, doi: [10.1190/1.1444302](https://doi.org/10.1190/1.1444302).
- Martins, C. M., V. C. Barbosa, and J. B. Silva, 2010, Simultaneous 3D depth-to-basement and density-contrast estimates using gravity data and depth control at few points: *Geophysics*, **75**, no. 3, I21–I28, doi: [10.1190/1.3380225](https://doi.org/10.1190/1.3380225).
- Portnaguine, O., and M. S. Zhdanov, 1999, Focusing geophysical inversion images: *Geophysics*, **64**, 874–887, doi: [10.1190/1.1444596](https://doi.org/10.1190/1.1444596).
- Portnaguine, O., and M. S. Zhdanov, 2002, 3-D magnetic inversion with data compression and image focusing: *Geophysics*, **67**, 1532–1541, doi: [10.1190/1.1512749](https://doi.org/10.1190/1.1512749).
- Shin, Y. H., C. K. Shum, C. Braitenberg, S. M. Lee, H. Xu, K. S. Choi, J. H. Baek, and J. U. Park, 2009, Three-dimensional fold structure of the Tibetan Moho from GRACE gravity data: *Geophysical Research Letters*, **36**, 58–69.
- Silva, J. B., D. C. Costa, and V. C. Barbosa, 2006, Gravity inversion of basement relief and estimation of density contrast variation with depth: *Geophysics*, **71**, no. 5, J51–J58, doi: [10.1190/1.2236383](https://doi.org/10.1190/1.2236383).
- Silva, J. B., W. E. Medeiros, and V. C. Barbosa, 2001, Potential-field inversion: Choosing the appropriate technique to solve a geologic problem: *Geophysics*, **66**, 511–520, doi: [10.1190/1.1444941](https://doi.org/10.1190/1.1444941).
- Wu, L., 2018a, Comparison of 3-D Fourier forward algorithms for gravity modelling of prismatic bodies with polynomial density distribution: *Geophysical Journal International*, **215**, 1865–1886, doi: [10.1093/gji/ggy379](https://doi.org/10.1093/gji/ggy379).
- Wu, L., 2018b, Efficient modeling of gravity fields caused by sources with arbitrary geometry and arbitrary density distribution: *Surveys in Geophysics*, **39**, 401–434, doi: [10.1007/s10712-018-9461-7](https://doi.org/10.1007/s10712-018-9461-7).
- Wu, L., and L. Chen, 2016, Fourier forward modelling of vector and tensor gravity fields due to prismatic bodies with variable density contrast: *Geophysics*, **81**, no. 1, G13–G26, doi: [10.1190/geo2014-0559.1](https://doi.org/10.1190/geo2014-0559.1).
- Xiao, F., and Z. Wang, 2017, Geological interpretation of Bouguer gravity and aeromagnetic data from the Gobi-desert covered area, Eastern Tianshan, China: Implications for porphyry Cu-Mo polymetallic deposits exploration: *Ore Geology Reviews*, **80**, 1042–1055, doi: [10.1016/j.oregeorev.2016.08.034](https://doi.org/10.1016/j.oregeorev.2016.08.034).
- Zhang, J., and L. Jiang, 2017, Analytical expressions for the gravitational vector field of a 3-D rectangular prism with density varying as an arbitrary-order polynomial function: *Geophysical Journal International*, **210**, 1176–1190, doi: [10.1093/gji/ggx230](https://doi.org/10.1093/gji/ggx230).
- Zhang, J., B. Zhong, X. Zhou, and Y. Dai, 2001, Gravity anomalies of 2-D bodies with variable density contrast: *Geophysics*, **66**, 809–813, doi: [10.1190/1.1444970](https://doi.org/10.1190/1.1444970).
- Zhang, L. C., M. G. Zhai, Y. S. Wan, J. H. Guo, Y. P. Dai, C. L. Wang, and L. Liu, 2012, Study of the precambrian BIF-iron deposits in the North China Craton: Progresses and questions (in Chinese with English abstract): *Acta Petrologica Sinica*, **28**, 3431–3445.
- Zhang, X., L. Zhang, P. Xiang, B. O. Wan, and F. Pirajno, 2011, Zircon U–Pb age, Hf isotopes and geochemistry of Shuichang Algoma-type banded iron-formation, North China Craton: Constraints on the ore-forming age and tectonic setting: *Gondwana Research*, **20**, 137–148, doi: [10.1016/j.gr.2011.02.008](https://doi.org/10.1016/j.gr.2011.02.008).
- Zhdanov, M. S., R. Ellis, and S. Mukherjee, 2004, Three-dimensional regularized focusing inversion of gravity gradient tensor component data: *Geophysics*, **69**, 925–937, doi: [10.1190/1.1778236](https://doi.org/10.1190/1.1778236).
- Zhou, X., 2008, 2D vector gravity potential and line integrals for the gravity anomaly caused by a 2D mass of depth-dependent density contrast: *Geophysics*, **73**, no. 6, I43–I50, doi: [10.1190/1.2976116](https://doi.org/10.1190/1.2976116).
- Zhou, X., 2009, General line integrals for gravity anomalies of irregular 2D masses with horizontally and vertically dependent density contrast: *Geophysics*, **74**, no. 2, I1–I7, doi: [10.1190/1.3073761](https://doi.org/10.1190/1.3073761).
- Zhou, X., 2010, Analytic solution of the gravity anomaly of irregular 2D masses with density contrast varying as a 2D polynomial function: *Geophysics*, **75**, no. 2, I11–I19, doi: [10.1190/1.3294699](https://doi.org/10.1190/1.3294699).